Evolution of wake structure around an impulsively stopped sphere with a streamwise magnetic field at $60 \leqslant \mathrm{Re} \leqslant 300$

Zheng-Gang Cai,* Jun-Hua Pan,* and Ming-Jiu Ni†
School of Engineering Science, University of Chinese Academy of Sciences, Beijing 101408, China

(Received 6 May 2022; accepted 18 November 2022; published 7 December 2022)

With a streamwise magnetic field, the evolution of wake structure in a flow around an impulsively stopped sphere in an incompressible viscous fluid is investigated. The research parameter range is $60 \leqslant \mathrm{Re} \leqslant 300$ and $0 \leqslant N \leqslant 10$, where Re and N are the Reynolds number and the interaction parameter, respectively. For present cases, the flow is fully developed before the sphere stopped and its symmetrical feature of the wake will be preserved after the sphere stopped. A complicated vortex structure system including a primary vortex ring, a fragmented secondary vortex, and an accompanying vortex is formed, which is summarized in a $\{N, \mathrm{Re}\}$ phase diagram. A scaling law of the drag force is found after the sphere stopped. It decays as $t^{*-2/3}$ at a small timescale and t^{*-1} or $t^{*-7/6}$ for different Reynolds numbers at a large timescale in the absence of a magnetic field, where t^* is the dimensionless time after abruptly stopping the sphere. When the magnetic field is applied, the decay rate of drag force is slower at a small timescale but faster at a large timescale. Meanwhile, peak azimuthal vorticity at the primary vortex ring core is shown to decay as $t^{*-4/3}$ at a large timescale when the flow is axisymmetric. It will decay faster under the influence of a streamwise magnetic field.

DOI: 10.1103/PhysRevFluids.7.123701

I. INTRODUCTION

The solid particle two-phase flow of fluid mechanics has been well studied by many researchers in the last few decades, since it is of great significance in fields of aerospace, ocean, and electromagnetic metallurgy engineering. As the basic flow among those, study of the accelerated or decelerated flow fields by an impulsively started or stopped solid particle has not received enough attention, although it has been applied widely in ballistics and multiphase fluid dynamics. Generally speaking, a solid particle is usually seen as a sphere or cylinder. For the accelerated flow of an impulsively started sphere in an incompressible fluid, Dennis and Walker [1] gave the evolution of drag coefficient and the flow separation time with different Reynolds numbers. Analytical results of Sano [2] and Lovalenti *et al.* [3] indicated that the history force decayed as $t^{*-1/2}$ at a small timescale with low Reynolds numbers. Here the dimensionless time t^* was scaled with the ratio of the sphere diameter to its constant velocity. The numerical study of Mei [4] also confirmed this decaying law with $\mathrm{Re} \leqslant 100$. Basset [5] noted that this force resulted from the diffusion of vorticity away from the sphere. Besides the sphere, research on the flow topological structure around an impulsively started cylinder was experimentally investigated in detail by Bouard and Coutanceau [6]. When Reynolds number $\mathrm{Re} = 60$ and $\mathrm{Re} = 500$, it was found that a bulge and an isolated secondary eddy appeared around the suddenly started cylinder, respectively, and the wake flow was divided into three different regimes according to Re. Koumoutsakos and Leonard [7] investigated

*These authors contributed equally to this work.
†mjni@ucas.ac.cn

the time-dependent drag coefficient of an impulsively started cylinder with a vortex method. It was found that the interaction between the cylinder with its primary or secondary wake vortices could cause the increase or decrease of drag. For the decelerated flow by an impulsively stopped body, relevant research is limited. When the stopped solid body is a cylinder, Wang and Dalton [8] reported the time history of the drag coefficient and found that changes of lift and drag forces on the cylinder were caused by induced velocities which were generated by initial wake vortices. Sheard *et al.* [9] gave trajectories of induced vortex pairs in the flow and used the Biot-Savart law to predict the curvature radius of their trajectories. As for the flow induced by a suddenly stopped sphere in an open fluid, there has been only a few research projects at very low Re like the work [10], in which the numerical investigation of decay of a drag coefficient was investigated at $\mathrm{Re} \leqslant 10$. It was found that the drag coefficient decayed slightly greater than $t^{*-1/2}$ at a small timescale. Furthermore, Lawrence and Mei [11] deduced that the transient drag force of the stopped sphere decayed as t^{*-1} at a large timescale by a global momentum balance for the new wake and the old one. It is noted that there is a close connection between the temporal force on the sphere and the evolution of wake structure.

Although, the decay of drag after stopping the sphere had been fully investigated at low Re, the wake structure of flow was not discussed. In the present paper, the evolution of wake structure around an impulsively stopped sphere is investigated in detail at $60 \leqslant \mathrm{Re} \leqslant 300$. According to the research [12], the upstream vortex ring will be developed in the downstream at large enough Re. But it should be noted that the flow dynamics in their work was induced by an impulsively stopped sphere traveling a short distance at $100 \leqslant \mathrm{Re} \leqslant 1500$ in the presence of a side wall. The flow before stopping the sphere was not fully developed. This is different from the present situation. The present cases consider an open fluid domain without a wall and a fully developed flow before stopping the sphere. For the present impulsively stopped body problem, this procedure involves the evolution of a vortex ring and its interaction with the stopped body. For research on the vortex ring, experimental studies of an individual vortex ring were performed by Maxworthy [13,14]. A classical entrainment model during the expansion of a laminar vortex ring was first reported in their work. The variation of vortex ring size a (the radius of the spheroidal vortex ring bubble measured by the center of a dyed ring in their experiments), velocity V_{ring}, and circulation Γ had been given by the model as

$$a \propto t^{*1/3}, V_{\mathrm{ring}} \propto t^{*-1}, \Gamma \propto t^{*1/3}. \tag{1}$$

The nondimensional variables, a, V_{ring}, and Γ were scaled with the sphere diameter, the sphere velocity and the product of both, respectively. The evolution of peak azimuthal vorticity in the vortex ring core was not measured in their experiments, which will be discussed in the present work. Furthermore, the vortex ring interaction with a free sphere was first experimentally studied by Allen *et al.* [15]. The velocity and acceleration of the moving sphere could be predicted by the integration of vorticity moment in the flow field.

As for the influence of magnetic field on the accelerated or decelerated flow by an impulsively started or stopped solid particle, there have been no studies to investigate the relevant problem. But for the flow past a fixed body under the influence of magnetic field, there is much relevant research. A uniform flow passing a fixed cylinder had been studied by Kolesnikov *et al.* [16] experimentally and Kanaris *et al.* [17] numerically, respectively. It was found that the axes of the wake vortices were parallel with the cylinder axis at a large interaction number N, when the magnetic field direction was aligned with the cylinder axis. Chester [18] first reported the drag coefficient formula of a sphere with a uniform flow passing by and neglecting the inertia term at a small magnetic field. Subsequently, an experimental study on the drag of a sphere in a conducting fluid was conducted by Yonas [19] with a streamwise magnetic field. It was found that the drag coefficient was proportional to the interaction number $N^{1/2}$ when a strong magnetic field was applied. Meanwhile, the drag coefficient was also investigated by Delacroix and Davoust [20] with a transverse magnetic field, and it was proportional to $N^{0.65}$ for a weak magnetic field. According to the recent research of Pan *et al.* [21] or Pan *et al.* [22] on the flow past a fixed sphere under the influence of a streamwise

or transverse magnetic field, the wake type would experience different topological structures and a "reversion phenomenon" was found, which meant that the wake structure behind the sphere at a higher Re with a certain N was corresponding to that at a lower Re with a smaller N. In addition, the drag coefficient of the sphere was found to be proportional to $N^{1/2}$ in the axisymmetric state when $N > 1$ with a streamwise magnetic field. While a transverse magnetic field was applied, it was proportional to $N^{2/3}$ at small N and $N^{1/2}$ at large N.

For further understanding the effect of a magnetic field on the decelerated flow, the flow around the sphere after it impulsively stopped will be investigated in the present work with a streamwise magnetic field. The evolution of the vortex ring and the decay of the drag coefficient will be discussed using direct numerical simulations in the wide range $60 \leqslant \mathrm{Re} \leqslant 300$ and $0 \leqslant N \leqslant 10$. The remainder of this paper is organized as follows. The numerical method is introduced in Sec. II. In Sec. III a detailed discussion on the vortex structure system after stopping the sphere is given with $60 \leqslant \mathrm{Re} \leqslant 300$. In Sec. IV the decay scaling laws of drag coefficient and peak azimuthal vorticity are investigated after the sphere stopped with $60 \leqslant \mathrm{Re} \leqslant 300$. Finally, a summary is given in Sec. V.

II. NUMERICAL METHOD

A sphere of diameter D is impulsively stopped after traveling a long distance L with a constant velocity U from rest in an electrical conducting incompressible Newtonian fluid. The density, kinematic viscosity, and electrical conductivity of fluid are represented by ρ, ν, and σ, respectively. A numerical method [23] is used here, which means that the velocity of fluid will be projected onto a translational moving frame fixed in the center of the traveling sphere. For most cases of solid particle two-phase liquid metal flow in industrial applications, the small length scale results in the magnetic Reynolds number $\mathrm{Re}_m = \mu\sigma UD \sim O(10^{-3}) \ll 1$. Here μ is the magnetic permeability. The magnitude of the magnetic Prandtl number is approximately $\mathrm{Pr}_m = \nu/\mu\sigma \sim O(10^{-5})$. Hence, a quasistatic approximation [24,25] is adopted, and nondimensional equations of flow with a magnetic field can be written as

$$\nabla \cdot \boldsymbol{u} = 0, \tag{2}$$

$$\frac{\partial \boldsymbol{u}}{\partial t} + [(\boldsymbol{u} - \boldsymbol{u}_s) \cdot \nabla]\boldsymbol{u} = -\nabla p + \frac{1}{\mathrm{Re}}\nabla^2 \boldsymbol{u} + N(\boldsymbol{J} \times \boldsymbol{B}_0), \tag{3}$$

$$\boldsymbol{J} = -\nabla\phi + \boldsymbol{u} \times \boldsymbol{B}_0, \tag{4}$$

$$\nabla \cdot \boldsymbol{J} = 0, \tag{5}$$

where nondimensional variables, velocity $\boldsymbol{u}$, time t, pressure p, sphere velocity $\boldsymbol{u}_s$, current density $\boldsymbol{J}$, uniform magnetic field $\boldsymbol{B}_0$, and electrical potential ϕ are scaled with U, D/U, ρU^2, U, $\sigma U B_0$, B_0, and DUB_0, respectively. Here B_0 represents the magnitude of vector $\boldsymbol{B}_0$. The Reynolds number and interaction parameter are given by $\mathrm{Re} = UD/\nu$ and $N = \sigma D B_0^2/\rho U$, respectively. They denote the ratio of inertia to viscous forces and the ratio of Lorentz to inertia forces, respectively. Also there is another dimensionless parameter, called the Hartmann number $\mathrm{Ha} = (N\mathrm{Re})^{1/2}$. It represents the ratio of Lorentz to viscous forces. According to the Ohm's law (4) and the solenoidal constraint on the electric current density (5), a Poisson equation for the electric potential can be written as

$$\nabla \cdot \nabla\phi = \nabla \cdot (\boldsymbol{u} \times \boldsymbol{B}_0). \tag{6}$$

A second-order accurate projection method is used to solve Eqs. (2)–(5). The convective and diffusion terms are both discretized using the semi-implicit Crank-Nicolson scheme. A consistent and conservative scheme is used to solve the electric potential Poisson equation. Detailed numerical procedures can be found in Ni *et al.* [26]. Flow configuration around a traveling sphere and corresponding geometrical parameters are presented in Fig. 1. As for boundary conditions, pressure and velocity are set fixed-value and zero-gradient boundary conditions at the upper surface. At

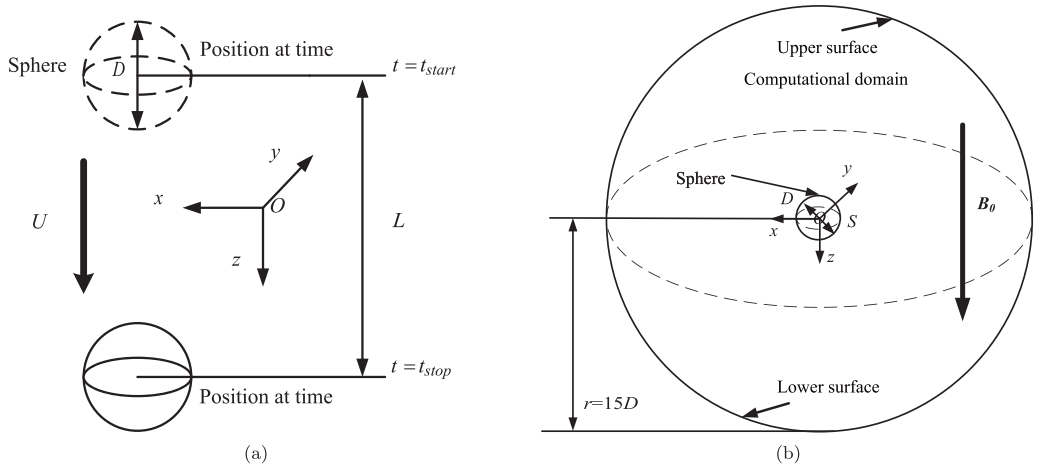

FIG. 1. Geometry configuration of flow. (a) The location of the sphere starting and stopping are shown by dashed and solid spheres, respectively. (b) The comoving frame is fixed in the center of the traveling sphere with the same translation velocity $\boldsymbol{u}_s$. The radius of spherical computational domain is set as $r = 15D$.

the lower surface, they are set zero-gradient and infinitely far boundary conditions. A no-slip boundary condition is applied on the traveling sphere. For magnetohydrodynamics (MHD) flows, a electrical potential governing equation needs to be considered. For the purpose of maintaining charge conservation in the fluid, the electrical potential boundary condition on the sphere is set as Mück *et al.* [27]

$$\frac{\partial \phi}{\partial n} = (\boldsymbol{u}_s \times \boldsymbol{B}_0) \cdot \boldsymbol{n}. \tag{7}$$

At the initial time ($t = t_{\text{start}} = 0$), the sphere is at rest in a quiescent fluid, and then it moves with a constant velocity U. After moving a long distance L, the sphere is abruptly brought to rest at time $t = t_{\text{stop}}$. A new time variable $t^* = t - t_{\text{stop}}$ is introduced. For cases in the present paper, L is set large enough to make the flow achieve a fully developed state. According to our experience, L is usually set as several hundred times the diameter of the sphere. After stopping the sphere, the evolution of wake structure around the sphere will be studied in detail in the range of numerical parameters $60 \leqslant \text{Re} \leqslant 300$ and $0 \leqslant N \leqslant 10$ or $0 \leqslant \text{Ha} \leqslant 54.8$. The maximal Reynolds number $\text{Re} = 300$ is chosen for grid independence tests. If one stands on the moving reference frame fixed on the sphere to observe the fully developed flow, there is no essential difference with the case of flow past a fixed sphere. When the magnetic field is absent, large-amplitude hairpin vortices are shed behind the sphere [29]. There are five different meshes to be applied for various situations. Due to the boundary layer caused by velocity shear between the sphere and the fluid, the grid resolution near the sphere should be paid more attention. A detailed grid independence study is examined for ensuring the accuracy of simulation. An O-type grid is set in the spherical computational domain to maintain a good grid orthogonality. The grid spacing of all meshes is increased with a ratio 1.1 away from the sphere surface. For different meshes, the distance between the nearest grid point and the sphere surface is set with $\delta_{\text{min}} = 0.01D$ and $\delta_{\text{min}} = 0.005D$. To solve the shear layer, four or five grid nodes are set in the boundary layer. Here the experience of previous works [21,22] is adopted. The thickness of the first layer is set as $0.01D$ at $N = 0$. When the magnetic field is imposed, the size will be reduced to $0.005D$. Furthermore, the size of computational domain is also tested with $r = 15D$ and $r = 30D$, respectively. Here the total cell number of all meshes is the same except mesh 1. Comparisons of the drag coefficient and Strouhal number at $t^* \leqslant 0$ with previous results are given in Table I. Results in the present work agree well with previous studies. According to results in Table I and considering the balance of computational cost and simulation accuracy, since

TABLE I. Grid independence test at Re = 300. δ is the first layer thickness of the sphere surface grid. C_d and S_t are the drag coefficient and the vortex-shedding frequency, which are scaled with $\frac{1}{2}\rho U^2 \pi D^2/4$ and U/D, respectively.

Cases	Radius of computational domain	Grid cells	C_d	S_t
Tomboulides and Orszag [28] (Re = 300)	—	—	0.671	1.36
Johnson and Patel [29] (Re = 300)	—	—	0.656	1.37
Pan *et al.* [21] (Re = 300, $N = 0$, $\delta_{\min} = 0.01D$)	—	1613038	0.665	1.36
Pan *et al.* [21] (Re = 300, $N = 10$, $\delta_{\min} = 0.01D$)	—	1613038	1.660	-
Mesh 1 (Re = 300, $N = 0$, $\delta_{\min} = 0.01D$)	$15D$	1406790	0.660	1.37
Mesh 2 (Re = 300, $N = 0$, $\delta_{\min} = 0.01D$)	$15D$	2457350	0.659	1.35
Mesh 3 (Re = 300, $N = 0$, $\delta_{\min} = 0.01D$)	$30D$	2457350	0.658	1.35
Mesh 2 (Re = 300, $N = 10$, $\delta_{\min} = 0.01D$)	$15D$	2457350	1.657(at $t^* = 0$)	-
Mesh 4 (Re = 300, $N = 10$, $\delta_{\min} = 0.005D$)	$15D$	2457350	1.656(at $t^* = 0$)	-
Mesh 5 (Re = 300, $N = 10$, $\delta_{\min} = 0.005D$)	$30D$	2457350	1.655(at $t^* = 0$)	-

the $r = 30D$ larger-domain results are almost indistinguishable from those at $r = 15D$, mesh 2 and mesh 4 are, respectively, adopted for present investigations without and with a streamwise magnetic field, which are sufficient to capture the evolution of flow structure.

III. FLOW AROUND THE STOPPED SPHERE AT $60 \leqslant \mathrm{Re} \leqslant 300$

A flow caused by a moving sphere is not essentially different from the uniform flow past a fixed sphere at $60 \leqslant \mathrm{Re} \leqslant 300$. So the detailed flow structure before a stopped sphere is not discussed here, but can be found in Johnson and Patel [29] in the absence of a magnetic field or in Pan *et al.* [21] with a streamwise magnetic field. It is easily found that the flow wake structure before a stopped sphere can be classified into three general types: steady axisymmetric flow, steady plane symmetric flow, and unsteady plane symmetric flow at $60 \leqslant \mathrm{Re} \leqslant 300$, $0 \leqslant N \leqslant 10$. In this section, influences of viscosity and magnetic field on the evolution of vortex ring after the sphere stopped will be investigated with $60 \leqslant \mathrm{Re} \leqslant 300$ and $0 \leqslant N \leqslant 10$. The flow is fully developed before the sphere stopped.

A. Wake structure around the stopped sphere at $N = 0$

A primary vortex ring will be made from the upstream after the sphere stopped. Flow patterns are shown in Fig. 2 at three representative Reynolds numbers in term of the flow symmetric characteristic without a magnetic field. Vortex structures highlighted by dimensional azimuthal vorticity ω_θ isosurfaces and their corresponding vorticity contours are presented at the same time $t^* = 6$. The reason to choose three such Reynolds numbers Re = 200, Re = 250, and Re = 300 is that they are representative of the steady axisymmetric wake, the steady plane symmetric state, and the periodic vortex shedding at $t^* < 0$, respectively. One can refer to Johnson and Patel [29] to understand the streamline of the flow before the sphere stopped. Here results of low Re corresponding to Model I in Fig. 3(b) are not presented. This flow pattern will be discussed in the next subsection with a magnetic field. All five types of the flow are summarized in Fig. 3, which is a brief model diagram for vortex structures. For better understanding flow patterns around the stopped sphere at $t^* > 0$, the model diagram is provided at the beginning, not the end, of this section. At Re = 200, an axisymmetric primary vortex ring with an elliptic cross section forms in Fig. 2(a), which corresponds to Model II in Fig. 3(c). The isolated primary vortex ring will keep moving downstream until it totally disappears because of the effect of viscous diffusion. With its

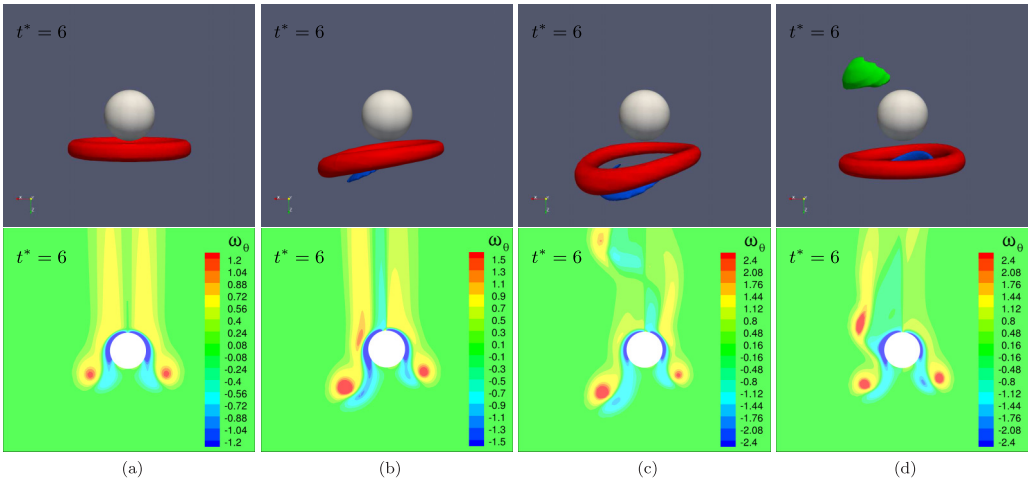

FIG. 2. Azimuthal vorticity ω_θ isosurface of vortex structures and corresponding vorticity contours in the symmetric plane at $t^* > 0$. The primary vortex ring, secondary vortex B, and accompanying vortex A are represented by red, blue, and green, respectively. The stopped sphere is expressed by a white geometry. (a) Re $= 200$; (b) Re $= 250$; (c) Re $= 300$, $t_{\text{stop}} = 0T$; (d) Re $= 300$, $t_{\text{stop}} = 2/4T$.

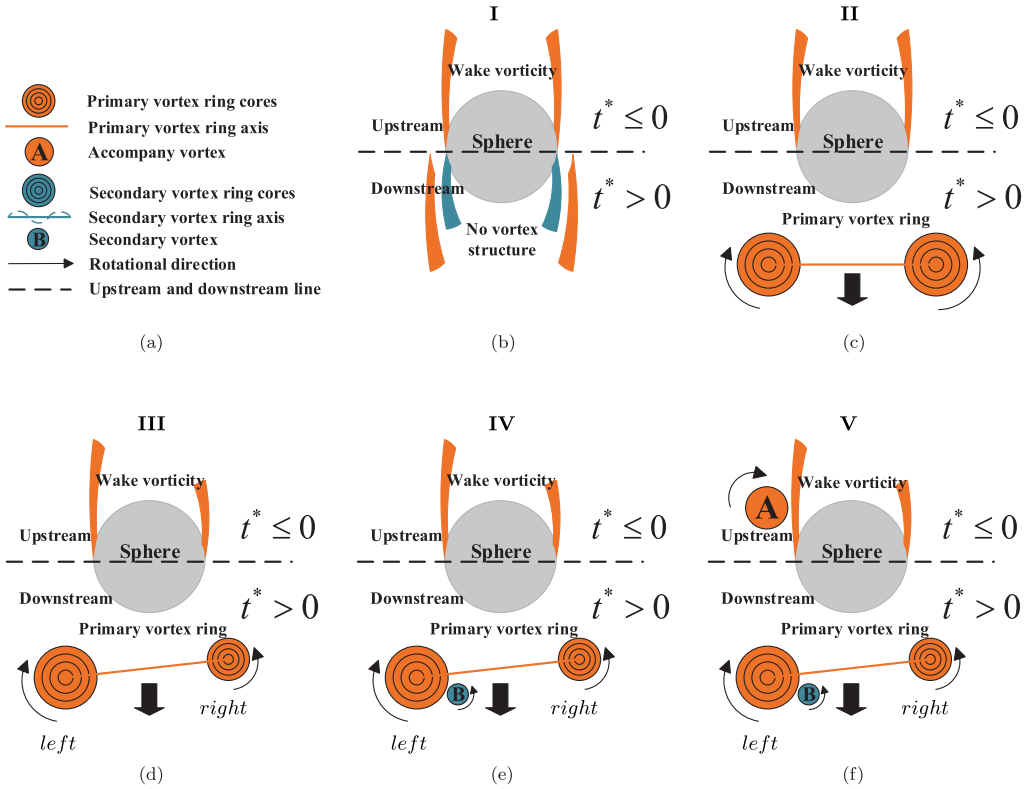

FIG. 3. A scheme diagram model for vortex structures near the sphere at $60 \leqslant \text{Re} \leqslant 300$. (a) Legend; (b) Model I: no vortex structure; (c) Model II: axisymmetric primary vortex ring; (d) Model III: inclined primary vortex ring; (e) Model IV: inclined primary vortex ring with secondary vortex B; (f) Model V: inclined primary vortex ring with vortex B and A.

corresponding vorticity contours, two symmetrical positive vorticity centers on the left and right sides of the sphere represent primary vortex cores. Both locations will be recorded for analyzing the trajectory of the vortex ring later. Moreover, as the upstream vortex passing over the sphere surface forms the primary vortex ring, the opposite-sign secondary vorticity generated at the surface in the downstream region will be stretched with the movement of the primary vortex ring. Now, the intensity of the primary vortex ring is not large enough. So the secondary vorticity is not shed from the sphere surface to form a secondary vortex structure.

When $\mathrm{Re} = 250$, before impulsively stoping the sphere, its wake is in a plane symmetric state. It is found that the symmetric plane will be unchanged after the sphere stopped. An inclined primary vortex ring with two asymmetric cores of different sizes in the left and right sides is generated in Fig. 2(b). In addition, a fragmented secondary vortex B appears near the primary vortex ring, and it is much smaller comparing with the primary one. The nonuniform distribution of upstream vorticity in the symmetric plane leads to the appearance of the inclined primary vortex ring. So the secondary vortex B can occur near the stronger left core, not the right one, which will be disappeared faster owing to its weaker intensity. Furthermore, the angle of inclination of the primary vortex ring almost keeps unchanged as it travels, which is approximately equal to 10.8°. The flow pattern is summarized as Model IV in Fig. 3(e). It is noted that Model III can be observed only with a magnetic field, which will be investigated in the next subsection.

A similar phenomenon is also found at $\mathrm{Re} = 300$ in Figs. 2(c) and 2(d). In view of the unsteady flow with a vortex-shedding period T at $t^* \leqslant 0$, the stopping time t_{stop} will be set to different values like $t_{\mathrm{stop}} = 0T$ and $t_{\mathrm{stop}} = 2/4T$. It is obviously found that a new accompanying vortex A appears above the primary vortex ring at $t^* = 6$ in Fig. 2(d). This is formed from the upstream trailing vortex that has been shed before the sphere stopped. The accompanying vortex A also will appear near the sphere at a larger time t^* in the case of $t_{\mathrm{stop}} = 0T$ at $\mathrm{Re} = 300$, since it is shed far from the sphere at the moment. This can be inferred from corresponding vorticity contours in Fig. 2(c). The angle of inclination of the primary vortex ring is also different with $\theta = 11.9^\circ$ at $t_{\mathrm{stop}} = 0T$ and $\theta = 0.08^\circ$ at $t_{\mathrm{stop}} = 2/4T$, which implies that the angle of inclination θ is dependent on the stopping time t_{stop}. In addition, the secondary vortex B also appears on the right side at $\mathrm{Re} = 300$ in Fig. 2(d). This is because the vorticity distribution is almost uniform on both sides, which are strong enough to roll up the secondary vortex. Both situations are summarized as Model V, in which the secondary vortex B is present only on the left side, since there is essentially no difference from the perspective of wake structure.

Next, time evolution of primary vortex ring core trajectories for radial and axial displacements in the symmetric plane will be studied quantitatively. It should be noted that the instantaneous position of the primary vortex ring core is scaled with the sphere diameter D. In Fig. 4(a) axisymmetric results are presented at $100 \leqslant \mathrm{Re} \leqslant 200$. It is found that trajectories tend to be more parallel to the z axis with increasing the Reynolds number. The motion of the primary vortex ring can be predicted by the self-induced velocity from the Biot-Savart law. Its radial velocity component is affected by the opposite-sign secondary vorticity induction near the sphere surface, while its axial velocity component is produced by the primary vortex ring self-induction. With increasing Re, the increment of intensity of the primary vortex ring is larger than that of secondary vorticity. Hence, the self-induced velocity component in the z direction becomes larger than the induced velocity in the r direction. In the lower part of Fig. 4(a), the r and z direction positions are provided as a function of time t^*. An approximate linear relationship is observed between vortex core displacement X with logarithm of time $\log(t^*)$ at $t^* > 1$, which can be simply written as $X = C_1 \log(t^*) + C_2$. Here C_1 and C_2 are constant and independent of time. Since the velocity of vortex core $V_{\mathrm{ring}} \equiv dX/dt = C_1 t^{*-1}$, it suggests that the corresponding r and z velocity components of the primary vortex ring movement decay at an algebraic rate t^{*-1}. Surprisingly, it is consistent with Maxworthy experimental results [13] $V_{\mathrm{ring}} \propto t^{*-1}$ on an isolated vortex ring case, which was also derived by an entrainment model analysis in his work.

Considering the asymmetry of primary vortex ring at $220 \leqslant \mathrm{Re} \leqslant 260$, trajectories of primary vortex ring will be recorded in both sides in Fig. 4(b). Although the change of trajectory is

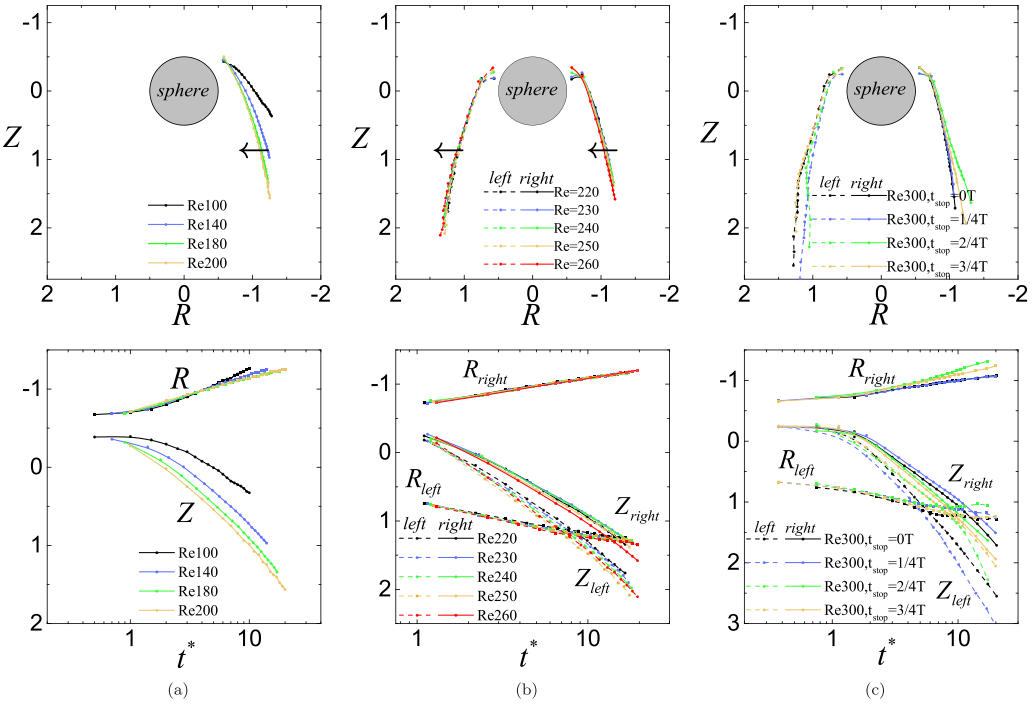

FIG. 4. The time evolution of primary vortex ring core trajectory for radial and axial displacements in the symmetric plane. The left and right cores are shown with dashed lines and solid lines, respectively. (a) $100 \leqslant \mathrm{Re} \leqslant 200$; (b) $220 \leqslant \mathrm{Re} \leqslant 260$; (c) $\mathrm{Re} = 300$ and $t_{\mathrm{stop}} = 0, 1/4T, 2/4T, 3/4T$.

comparatively small with Re increasing, it is found that the left trajectory is away from the sphere while the right trajectory is close to it slightly. The variation tendency of trajectory on the right side is the same as that of axisymmetric cases, while it is different on the left side. As mentioned above, there is a secondary vortex B due to the nonuniform distribution of upstream vorticity, which is enhanced as Re increasing. It means that the intensity of secondary vorticity rolled by the primary vortex ring will be much stronger on the left side than that on the right side. Then the radial induced velocity component is increased due to the secondary vortex B in the left core compared with that in the right core or axisymmetric cases without a secondary vortex B. So the left trajectory of the primary vortex ring core keeps away from the sphere. Comparing the time evolution of the primary vortex ring core, it is found that both radial and axial displacements are linearly dependent on logarithm of time, and the growth rate of displacement along the axial direction in the left core is larger than that in the right one. In Fig. 4(c) four results are recorded with different stopping times t_{stop} during a whole period T in consideration of a periodical vortex-shedding phenomenon at $\mathrm{Re} = 300$. It is obvious that the motion of the primary vortex ring is very different because the upstream wake vorticity distribution changes with different stopping times t_{stop}. Furthermore, time-varying radial and axial displacements of the primary vortex ring core at $\mathrm{Re} = 300$ are also presented in the lower part of Fig. 4(c), and the approximate linear relationship still exists at $t^* > 1$, which means that the velocity of the primary vortex ring is approximatively proportional to t^{*-1}.

B. Wake structure around the stopped sphere at $0 < N \leqslant 10$

The influence of a magnetic field on the evolution of azimuthal vorticity ω_θ is investigated with a fixed Reynolds number $\mathrm{Re} = 300$ in Fig. 5, where the magnetic field is imposed from the beginning ($t = 0$). At $N \geqslant 1$, no vortex structure exists and the vorticity has always been suppressed near the

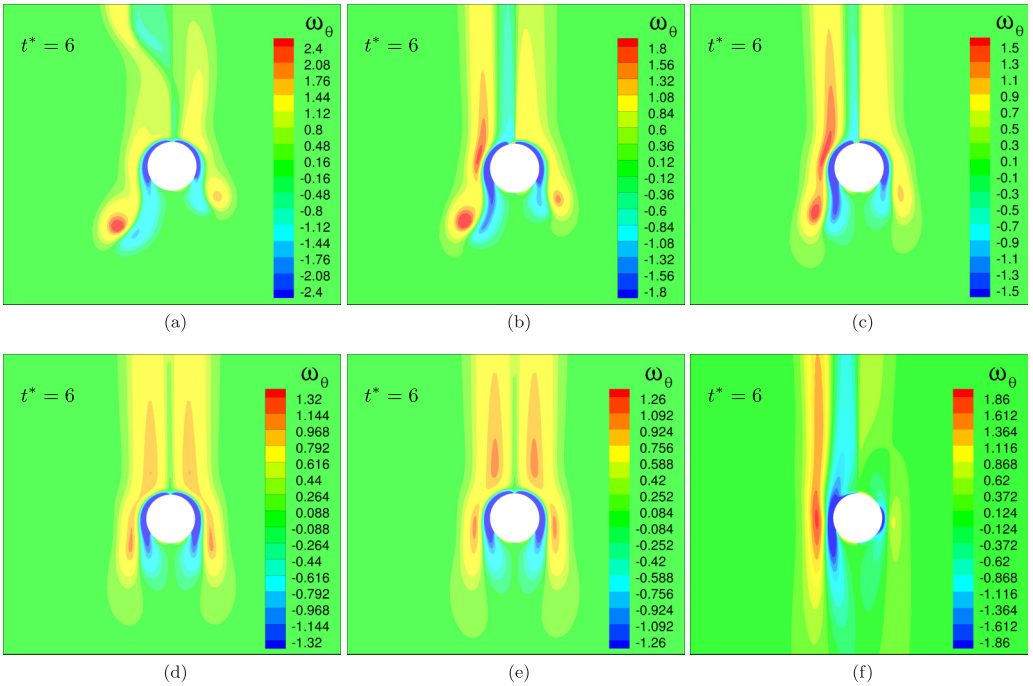

FIG. 5. Azimuthal vorticity ω_θ contours in the symmetric plane with Reynolds number Re $= 300$ at various time instances when the magnetic field is applied. (a) Re $= 300$, $N = 0.1$; (b) Re $= 300$, $N = 0.25$; (c) Re $= 300$, $N = 0.5$; (d) Re $= 300$, $N = 0.75$; (e) Re $= 300$, $N = 1$; (f) Re $= 300$, $N = 6.25$.

equator of the sphere at $z \approx 0$. For convenience of judgment whether a primary vortex ring is shed from the sphere surface or not, a unified standard is proposed whether the axial position for local positive extremum of vorticity can be reached at $z = 0.25D$ or not. This judgment is also adopted in the absence of a magnetic field case.

Comparing with azimuthal vorticity contours at Re $= 300$ with $N = 0$, similar results are found at a small interaction number $N = 0.1$ in Fig. 5(a). The flow pattern can be regarded as Model V in Fig. 3(f). Referring to our previous work about MHD flows past a fixed sphere [21], with $N = 0.25$ in Fig. 5(b), the flow at $t^* \leqslant 0$ becomes steady plane symmetric, which means that the accompanying vortex A will disappear under the influence of the magnetic field. The secondary vortex B has occurred at $3 < t^* < 6$, although it is dissipated at the $t^* = 6$. This flow pattern is seen as Model IV. Its corresponding radial Lorentz force LF_r contour in the symmetric plane is also presented in Fig. 6(a). As shown in Fig. 3, considering the circular movement of the primary vortex ring core in the symmetric plane, at the upper part of the primary vortex ring core, the inward radial velocity component of fluid is damped by the outward Lorentz force, while the outward radial velocity component of fluid is damped by the inward Lorentz force at its bottom part. Consequently, both inverse actions result to the elliptic vortex ring being flatter, even vanished with increasing N. At $N = 0.5$ in Fig. 5(c), vortex structures A and B both vanish except the inclined primary vortex ring. This wake structure is not found in the situation without a magnetic field, which is regarded as a new Model III in Fig. 3(d). The sole primary vortex ring becomes axisymmetric in Fig. 5(d) at $N = 0.75$. This situation exactly corresponds to Model II. In addition, its corresponding radial Lorentz force LF_r contours are presented in Fig. 6(b). Comparing with that at $N = 0.25$, the position of the maximum outward Lorentz force has changed, which is closer to the sphere. It means that the the primary vortex ring core is confined near the sphere. The flow is still axisymmetric at $N = 1$, but now there is no primary vortex ring formed. The major vorticity is confined to the sphere surface due to the strong Lorentz force in Fig. 5(e), which is very similar to the result of low Re without

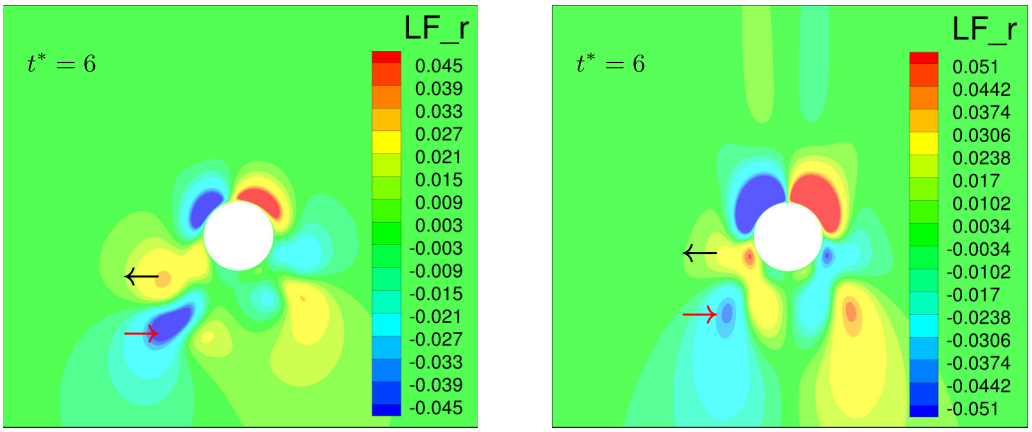

FIG. 6. The radial Lorentz force LF_r contours at Re = 300. The direction of Lorentz force in the orange red region is indicated as a black arrow (away from the sphere), and that in the blue region is shown as a red arrow (close to the sphere). (a) Re = 300, $N = 0.25$, LF_r; (b) Re = 300, $N = 0.75$, LF_r.

a magnetic field. The flow pattern is seen as Model I. When $N = 6.25$, the upstream wake flow becomes a plane symmetric pattern, which has been found and explained by Pan *et al.* [21]. There is also no vortex structure formed in the downstream in Fig. 5(f) like the flow at $N = 1$. So this situation also belongs to Model I.

Time evolution of the primary ring core trajectory for radial and axial displacements in the symmetric plane is also investigated quantitatively with different magnetic fields at Re = 300 in Fig. 7. Here the maximum interaction number N is 0.75, since there is no vortex ring when $N \geqslant 1$. The data only in the right core are presented by considering the axisymmetric characteristic of flow

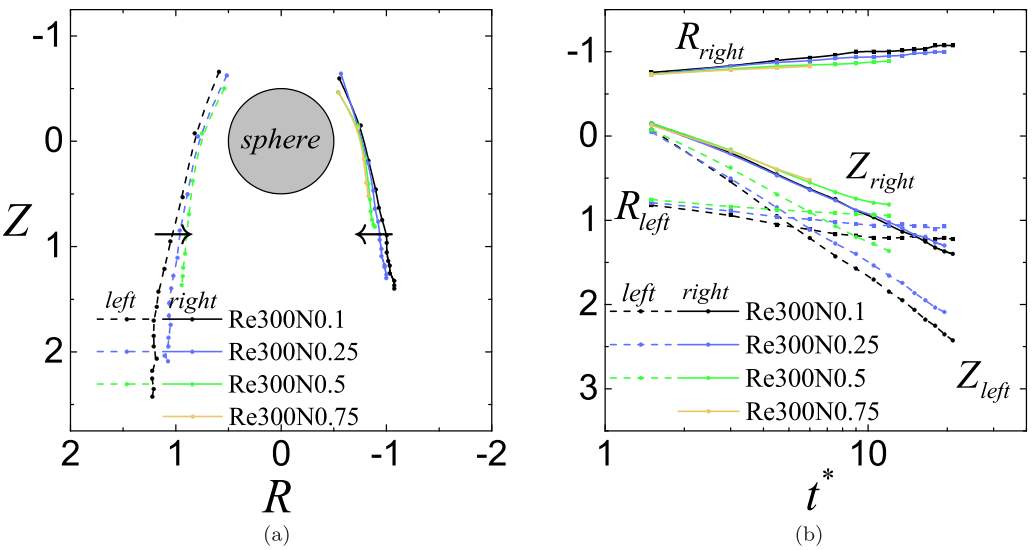

FIG. 7. The time evolution of primary ring core trajectory for radial and axial displacements in the symmetric plane with different interaction number N at Re = 300. The left and right cores are described by dashed lines and solid lines, respectively. (a) Trajectories; (b) time-varying displacement.

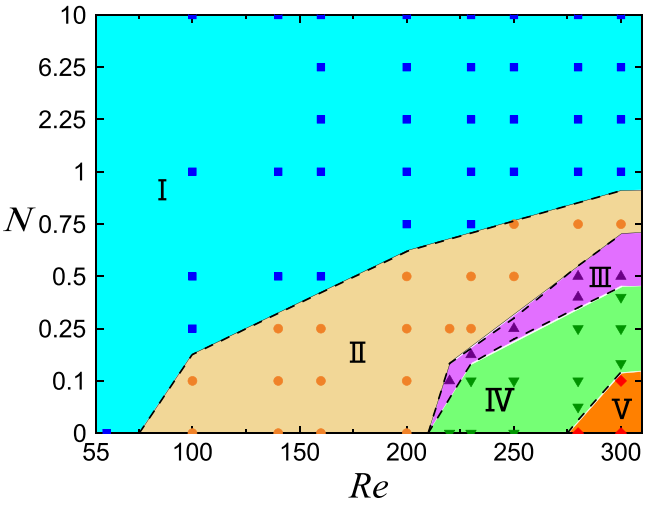

FIG. 8. A simple map with wake patterns around a stopped sphere in the plane $\{N, \mathrm{Re}\}$. It is divided into five regimes called I, II, III, IV, and V. They correspond to the five flow patterns in Fig. 3. The flow patterns in regimes I, II, III, IV, and V belong to Models I, II, III, IV, and V, respectively.

at $N = 0.75$. Any flow which is not parallel to the magnetic field will be damped by the Lorentz force under the influence of a streamwise magnetic field. As shown in Fig. 7, the primary vortex ring diameter decreases as increasing N until there is no primary vortex ring forming owing to the stronger Lorentz force. In Fig. 7(b) the linear relationship between primary ring core displacement and logarithm of time $\log(t^*)$ is consistent with the situation at $N = 0$ whether in the radial or axial direction. It means that the velocity of vortex core motion still decays at an algebraic rate t^{*-1}, even affected by a streamwise magnetic field. The inclined lines of the trajectory on Z_{right}, R_{right}, Z_{left}, and R_{left} all descend as increasing N with a fixed Reynolds number $\mathrm{Re} = 300$. This indicates that the velocity of primary ring is reduced with a stronger magnetic field.

C. Summary of wake flow patterns at $60 \leqslant \mathrm{Re} \leqslant 300$, $0 \leqslant N \leqslant 10$

According to the model diagram in Fig. 3, a simple map is presented in the plane $\{N, \mathrm{Re}\}$ in Fig. 8, which distinguishes five different wake flow patterns based on the existence of a primary vortex ring, fragmented secondary vortex B, and accompanying vortex A. For Model I, there is no vortex structure appearing at $t^* > 0$. In Model II, a sole axisymmetric primary vortex ring will form in the downstream at $t^* > 0$ and by the axisymmetric wake vorticity in the upstream at $t^* \leqslant 0$. The sole primary vortex ring will be inclined in certain Re and N like in Model III. For Model IV, a small secondary vortex structure B with opposite-sign vorticity will detached from the sphere surface and move around the primary vortex ring. The far accompanying vortex structure A in the upstream approaches the stopped sphere at $t^* > 0$ in Model V and three kinds of vortex structures can be captured, for which the wake flow around sphere is the most complicated. In the model diagram, it is found that the secondary vortex B appears only in the plane symmetric flow, since the primary vortex should be strong enough to roll the second vortex B up from the secondary vorticity on the sphere surface. For cases at a higher Reynolds number like $\mathrm{Re} = 300$, the secondary vortex B may appear on both sides because of different stopping times. As for the vortex A, its appearance is essentially related to that whether the flow is unsteady to generate a shedding vortex at $t^* \leqslant 0$. Furthermore, a so-called "reversion phenomenon" is found by Pan *et al.* [21] for a uniform flow past a fixed sphere with a streamwise magnetic field. A similar phenomenon is also found on the flow pattern in the downstream at $t^* > 0$. It means that the flow pattern with a higher Reynolds number

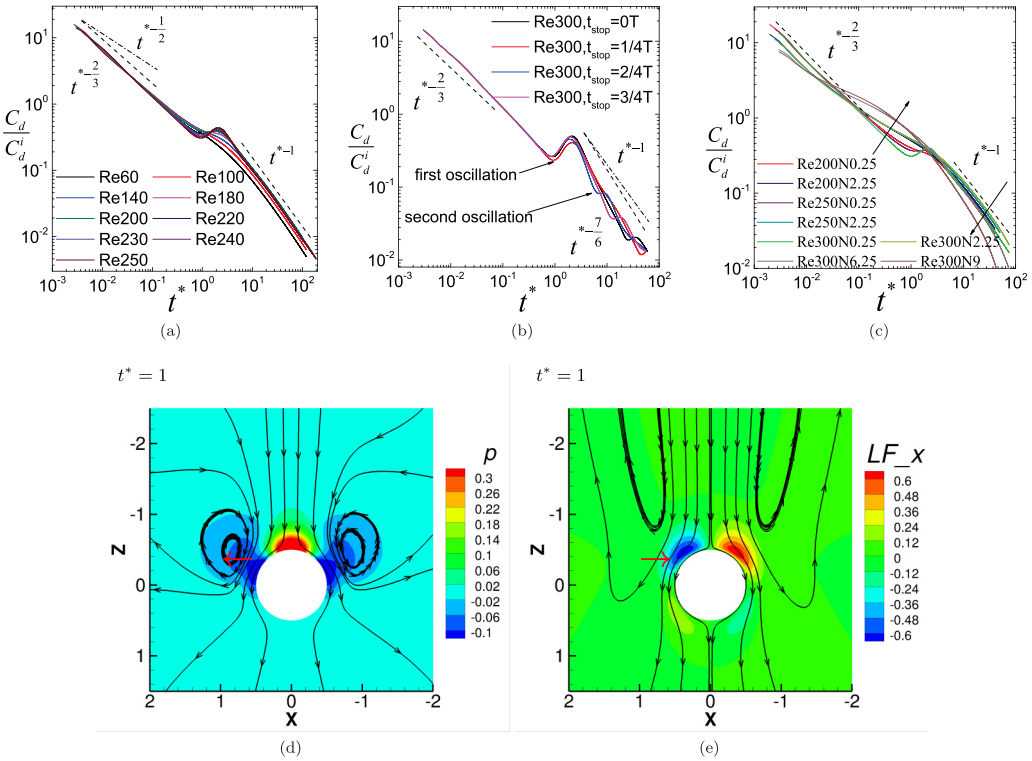

FIG. 9. The variation of normalization drag coefficient $\tilde{C}_d = C_d/C_d^i$ over time at different Re and N ranges. The drag coefficient C_d is normalized with the average drag coefficient C_d^i at $t^* \leqslant 0$. (a) $60 \leqslant \mathrm{Re} \leqslant 250$ with $N = 0$; (b) $\mathrm{Re} = 300$, $0T \leqslant t_{\mathrm{stop}} \leqslant 3/4T$ with $N = 0$; (c) $\tilde{C}_d$ with different N; (d) instantaneous streamline at $\mathrm{Re} = 200$, $N = 0$; (e) instantaneous streamline at $\mathrm{Re} = 200$, $N = 2.25$.

Re and a higher interaction number N corresponds to that with a lower Reynolds number Re and a lower interaction number N.

IV. DECAY OF DRAG AND PEAK AZIMUTHAL VORTICITY AT $60 \leqslant \mathrm{Re} \leqslant 300$

In this section, scaling laws about the decay of normalization drag coefficient $\tilde{C}_d = C_d/C_d^i$ of the stopped sphere and magnitude of peak azimuthal vorticity $|\Omega_\theta|$ in the primary vortex core will be investigated at $60 \leqslant \mathrm{Re} \leqslant 300$ with a streamwise magnetic field. Here C_d^i is the average drag coefficient before the sphere stopped.

A. Decay of drag coefficient

A normalization drag coefficient $\tilde{C}_d$ of the impulsively stopped sphere is plotted at $t^* > 0$ in Fig. 9. In Fig. 9(a) the result at $60 \leqslant \mathrm{Re} \leqslant 250$ with $N = 0$ is presented, for which the flow around the sphere is steady at $t^* \leqslant 0$. A distinctive fact is found that $\tilde{C}_d \propto t^{*-2/3}$ at the initial stage $t^* < 1$ and as t^{*-1} at the large timescale stage $t^* > 1$. The former at a small timescale is similar with the result in the study [10] about the flow around an impulsively started sphere at $\mathrm{Re} \leqslant 10$. A qualitative conclusion that the decay of $\tilde{C}_d$ is greater than $t^{*-1/2}$ was found by their numerical simulations, but a quantitative scaling law was not given. Since no analytical solution of the force of impulsively stopped sphere at a small timescale is given and considering the similarity between it and the problem on an impulsively started sphere, the scale law $\tilde{C}_d \propto t^{*-2/3}$ can be explained

qualitatively from the flow field near the sphere. According to the study on the force of impulsively started sphere of Mei [4], a decay of the history force as $t^{*-1/2}$ at a small timescale, which is obtained by subtracting the quasisteady drag from the computed total drag, has been proved. In the present paper, the quasisteady drag of the stopped sphere is zero. The main difference of these two situations at the initial stage $t^* < 1$ is that there is a primary vortex ring near the sphere in the upstream as shown in Fig. 9(d). It should be noticed that streamlines are pulled away from the sphere because the induction of the primary vortex ring increases the outward velocity of fluid near the sphere surface. The shear action between fluid and the sphere is weakened, which results in a faster decay than $t^{*-1/2}$ on the drag force.

The scale law t^{*-1} at a large timescale has been first provided by Lawrence and Mei [11], where an assumption without lift is taken in their theoretical model. Surprisingly, this conclusion is still valid for the plane symmetric case, for which the flow is steady at $t^* < 0$. Meanwhile, an oscillation occurs at $t^* \approx 1$, which is associated with the primary vortex ring motion. An obvious negative pressure on the sphere surface corresponding to the primary vortex ring is shown in Fig. 9(d). The oscillation of drag force is caused by the movement of the negative pressure from up surface to down surface of the sphere. Furthermore, the amplitude of oscillation is determined by the amplitude of negative pressure, which corresponds to the intensity of primary vortex ring. The oscillation will decrease even disappear as decreasing Re, as shown in Fig. 9(a). It is because that the intensity of the primary vortex ring is proportional to the Reynolds number. At $\mathrm{Re} = 300$, four cases with different stopping times t_{stop} during a period T of vortex shedding are presented in Fig. 9(b). It is found that the decay law as $t^{*-2/3}$ at the initial stage still exists, but the normalization drag coefficient $\tilde{C}_d$ of large timescale decays faster than t^{*-1}. According to Model V in Fig. 3(f), an accompanying vortex A, which possesses the same sign vorticity with the primary vortex ring, will form in the upstream. So streamlines near the sphere surface are further pulled away as the accompany vortex A approaching the sphere in the upstream region at $t^* \gg 1$. The shear action between fluid and the sphere is further weakened, which leads to a faster decay rate than t^{*-1}. In addition, a secondary oscillation occurring on $\tilde{C}_d$ curve will appear, when the accompanying vortex A moves from upstream to downstream like the primary vortex ring. So the occurring time of secondary oscillation for different t_{stop} is various, which corresponds to the impact time of accompanying vortex A on the sphere. In conclusion, the first and secondary oscillations are caused by motions along the sphere surface of the primary vortex ring and the accompany vortex A, respectively.

Basset [5] used the classical Stokes equations to derive a history force for the motion of a sphere, whose kernel decayed as $t^{*-1/2}$. This force arises due to the diffusion of vorticity generated at the surface of the sphere into the bulk flow. Sano [2] considered the force on a sphere in an impulsively started motion at small Reynolds number by the method of matched asymptotic expansions, at which the force decays much more quickly as t^{*-2} at its long-time behavior. It is of interest to note that with the inclusion of the Oseen convective inertia, the force decays as t^{*-2} in contrast to the $t^{*-1/2}$. Lovalenti *et al.* [3] reported that at finite Reynolds number, the vorticity had diffused out to the Oseen distance $(\nu t^*)^{1/2}$, which would be transported by convection. This difference in the mechanism of vorticity transport accounted for the change in the temporal behavior of the history force. An impulsively stopped motion is much different than the impulsively started one. Here, after the sphere is stopped, a large eddy is formed to the side of the sphere in Fig. 9(d), which will be transported by convection and result in a faster decay $t^{*-2/3}$ than $t^{*-1/2}$ in Fig. 9(a) at a small timescale. It seems that convection effect of the high Reynolds number has a contribution to the drag force apart from the one resulting from the Stokes flow.

For the impulsively stopped motion of the sphere, at the initial stage, assuming that one stands on the sphere to observe the flow, it seems like a flow past a sphere. Considering a flow past a sphere, Stokes drag $C_d = \frac{24}{\mathrm{Re}}$ is extended to Oseen drag $C_d = \frac{24}{\mathrm{Re}}(1 + \frac{3}{16}\mathrm{Re})$ with an Oseen approximation. However, rigorous analytical results are all restricted to zero or asymptotically small Reynolds number. Here, taking the form of the Oseen drag as a reference, empirical drag formulas are selected for high Reynolds number cases, such as $C_d = \frac{24}{\mathrm{Re}}(1 + 0.15\mathrm{Re}^{0.681})$ in Brown and Lawler

[30], $C_d = \frac{24}{\mathrm{Re}}(1 + 0.15\mathrm{Re}^{0.687})$ in Clift *et al.* [31], and $C_d = \frac{24}{\mathrm{Re}}(1 + 0.173\mathrm{Re}^{0.657})$ in Turton and Levenspiel [32], where the other correction term has been dropped because of its negligible value in the present Reynolds number range. From the Stokes drag to the Oseen drag formulas, it inspires us to note that the sphere drag can be divided into two parts, the Stokes drag $C_d^{\mathrm{Stokes}} = \frac{24}{\mathrm{Re}}$ part and the high Reynolds number convection effect correction part $C_d^{\mathrm{convection}} \sim \mathrm{Re}^{-1/3}$. For the impulsively stopped motion problem, since the vorticity should diffuse out to the Oseen distance $(\nu t^*)^{1/2}$, the convection effect can contribute to the drag force. So the Oseen distance is selected as a length scale in $C_d^{\mathrm{convection}}$, and the temporal behavior of the drag force at high Reynolds number for an impulsively stopped motion problem at the initial stage can be derived as $C_d^{\mathrm{convection}} \sim t^{*-1/6}$. It is noted that the motion of the large eddy in Fig. 9(d) will pull away streamlines from the sphere, which will weaken the shear action between fluid and the sphere. Hence, the convection effect $C_d^{\mathrm{convection}} \sim t^{*-1/6}$ should couple with the Stokes flow result $C_d \sim t^{*-1/2}$, which leads to the final temporal behavior of the drag force as $C_d \sim t^{*-1/2} t^{*-1/6} \sim t^{*-2/3}$. Furthermore, Lawrence and Mei [11] gave a scale law t^{*-1} at a large timescale through the application of global conservation principles. For $\mathrm{Re} = 300$ cases, a serious of accompanying vortices A are formed upstream before stopping the sphere and, they will continue to approach the sphere in the upstream region at $t^* \gg 1$ after stopping the sphere. Such an accompanying vortex will bring the convection effect, which results in a similar drag decay as $C_d^{\mathrm{convection}} \sim t^{*-1/6}$. This drag decay couples with the scale law t^{*-1} to lead to a scale law $t^{*-7/6}$ at a large timescale. Results in Figs. 9(a) and 9(b) show good agreement with present drag scaling law analysis.

Next, the effect of streamwise magnetic field is considered in Fig. 9(c). When a small magnetic field is applied like $N = 0.25$, the scaling laws of $t^{*-2/3}$ at the initial stage $t^* \leqslant 1$ and t^{*-1} at a large timescale $t^* \gg 1$ are almost same as that with $N = 0$. It is found that the rate of drag decay is decelerating at $t^* \leqslant 1$ and accelerating at $t^* \gg 1$ with increasing N. Meanwhile, the first oscillation of drag decay line at $t^* \approx 1$ caused by the motion of primary vortex ring also disappears as the primary vortex ring suppressed by a stronger magnetic field. These transformations are particularly prominent at a strong magnetic field. For further exploring the mechanism of action of magnetic field on drag decay after stopping the sphere, instantaneous streamlines at $t^* = 1$ with $\mathrm{Re} = 200$ and $N = 2.25$ are provided in Fig. 9(e). Comparing with the result in Fig. 9(d), the previous primary vortex ring near the sphere at $N = 0$ has been quickly suppressed due to the strong magnetic field. When the streamwise magnetic field is applied, there are two different effects on the shear action. First, the radial Lorenz force will suppress the radial outward flow, which will lead to the disappearance of the primary vortex ring. This effect will enhance the shear action between fluid and sphere, which will decelerate the decay of drag. Second, the kinetic energy of upstream inertial fluid is decreased by both the viscous dissipation and the Joule dissipation, which leads to the faster decrease of velocity of fluid past the stopped sphere. The shear action also will be decreased as the velocity decreased, which will accelerate the rate of drag decay. At a small timescale, the velocity loss of the inertial fluid is small. The first effect plays a major role on the drag decay, which leads to the rate of decay slower than $t^{*-2/3}$. But at a large timescale, the velocity of fluid past the stopped sphere has become small. Hence, the second effect plays a major role and leads to a faster decay rate than t^{*-1}.

B. Decay of peak azimuthal vorticity

The decay of the magnitude of peak azimuthal vorticity in the primary vortex core is quantitatively investigated at $60 \leqslant \mathrm{Re} \leqslant 300$ with a magnetic field. In Fig. 10(a) the time evolution of dimensionless peak azimuthal vorticity magnitude $|\Psi_\theta| = |\omega_\theta| D/U$ at the primary ring core in the symmetric plane is presented for axisymmetric cases. An interesting fact is found that the peak azimuthal vorticity $|\Psi_\theta|$ possesses a tendency of algebraic decay with an approximate timescale law $t^{*-4/3}$ at $\mathrm{Re} \leqslant 200$, for which the primary vortex ring is axisymmetric during its motion. Then a simple dimensional analysis is provided to explain the scaling law according to the well-known entrainment theory about the isolated vortex ring proposed by Maxworthy [13]. The variation of vortex size $a \propto t^{*1/3}$ and velocity $V_{\mathrm{ring}} \propto t^{*-1}$ have also been given by their model. It is noted

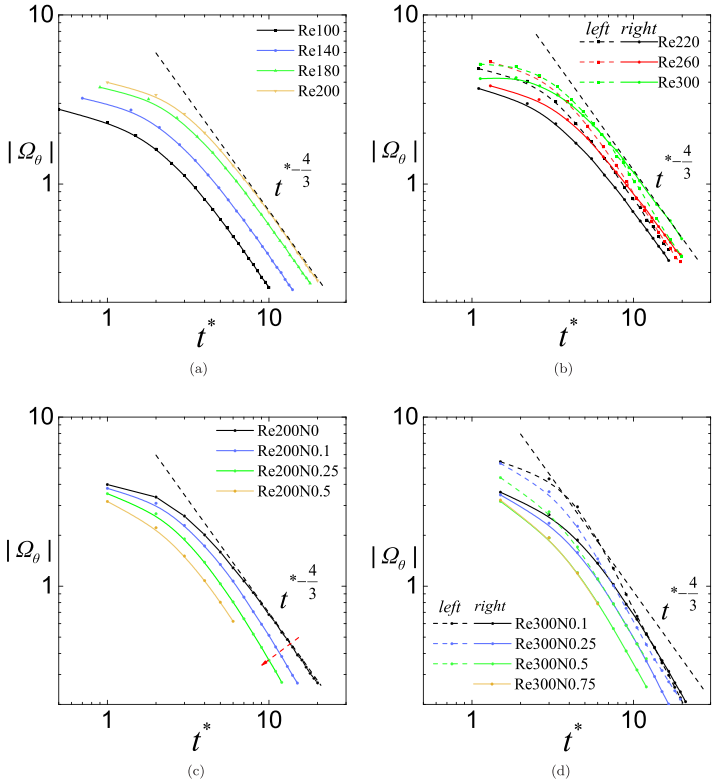

FIG. 10. The time evolution of dimensionless peak azimuthal vorticity at the center of the primary ring core in the symmetric plane. (a) $100 \leqslant \mathrm{Re} \leqslant 200$ with $N = 0$; (b) $220 \leqslant \mathrm{Re} \leqslant 300$ with $N = 0$; (c) $\mathrm{Re} = 200$ with different N; (d) $\mathrm{Re} = 300$ with different N.

that velocity $V_{\mathrm{ring}} \propto t^{*-1}$ has been confirmed in the present Sec. III A. According to dimensional analysis, the variation of peak azimuthal vorticity can be deduced as

$$|\Psi_\theta| \propto V_{\mathrm{ring}}/a \propto t^{*-4/3}. \tag{8}$$

Equation (8) agrees well with the present numerical results at $t^* > 1$. The conclusion is not valid at the initial stage $0 < t^* < 1$, since the primary vortex ring is developing, which has not been shed away from the sphere surface and leads to the failure of the entrainment model.

Next, results of plane symmetric cases are given in Fig. 10(b). Different decay rates of $|\Psi_\theta|$ on the left and right cores are obvious. The left one is faster than $t^{*-4/3}$, and the right one is slower. It should be noted that the decay of vorticty magnitude $|\Omega_\theta|$ is due to the viscous diffusion effect of fluid and the annihilation effect with concomitant opposite-sign vorticity generated at the sphere surface during the motion of primary vortex ring. In fact, the latter effect is not considered for deducing the decay scaling law $t^{*-4/3}$ in axisymmetric cases because it is absent in the previous entrainment theory for an isolated vortex ring motion. But an annihilation effect can be used to explain the phenomenon for vorticity decay in plane symmetric cases even with a magnetic field. At the initial stage, the stronger left core of the primary vortex ring rolls up stronger opposite-sign vorticity around itself. So the annihilation effect is stronger on the left core, which results in a faster decay compared the right one. The difference is more and more obvious as increasing Re.

The variation of dimensionless peak azimuthal vorticity $|\Psi_\theta|$ at the primary vortex ring core with a streamwise magnetic field is given in Figs. 10(c) and 10(d). In Fig. 10(c) the effect of magnetic field on the axisymmetric vortex ring is investigated. The decay rate of $|\Psi_\theta|$ with a magnetic field is

slightly faster than $t^{*-4/3}$. Because the vortex ring bubble is assumed to be a spheroid in entrainment theory, the assumption is no longer satisfied after the vortex ring is compressed by the Lorentz force. The theoretical model from the study [13] is not valid under the influence of a magnetic field. So the scaling law of peak azimuthal vorticity no longer satisfies $t^{*-4/3}$. Meanwhile, comparing four contours among Fig. 5(a), 5(b), 5(c), and 5(d), it can be found that the primary (positive) vorticity and secondary (negative) vorticity are decreased as increasing N, but the primary vorticity is decreased more than the secondary one. This is equivalent to enhancement of the annihilation effect of secondary vorticity, which means that the decay rate of $|\Psi_\theta|$ becomes faster than that at $N = 0$. It is more obvious at $\mathrm{Re} = 300$, $N > 0$, for which the decay rate of $|\Psi_\theta|$ in both cores is much faster than $t^{*-4/3}$.

V. SUMMARY

Flow dynamics around an impulsively stopped sphere after traveling a sufficiently long distance with a constant velocity have been investigated numerically both without and with a streamwise magnetic field. For cases of Reynolds number $60 \leqslant \mathrm{Re} \leqslant 300$, a complicated vortex structure system will form, which consists of primary, fragmented secondary, and accompanying vortex structures. According to the presence of these three kinds of vortex structures, a simple map of regimes for wake flow patterns is given in the $\{N, \mathrm{Re}\}$ plane. Due to the inheritance feature of the flow symmetry at $t^* > 0$, the primary vortex ring will reserve an axisymmetric state or a plane symmetric state. Whether there is a magnetic field or not, an approximate linear relationship between the displacement of primary vortex core and logarithmic of time $\log(t^*)$ is found. Furthermore, a "reversion phenomenon" is also found, which means that the flow pattern with a higher Reynolds number Re and a higher interaction number N corresponds to that with a lower Reynolds number Re and a lower interaction number N.

Meanwhile, the decay of drag coefficient after the sphere stopped is also investigated with $60 \leqslant \mathrm{Re} \leqslant 300$ and $0 \leqslant N \leqslant 10$. At the initial stage, the normalization drag coefficient $\tilde{C}_d$ will decay at an algebraic rate of $t^{*-2/3}$ with $60 \leqslant \mathrm{Re} \leqslant 300$ and $N = 0$. The speed of decay will approach t^{*-1} or $t^{*-7/6}$ for different Reynolds numbers at a large timescale after experiencing a small oscillation, which is caused by the primary vortex ring. With increasing N, the decay rate of drag force will become slower at a small timescale but faster at a large timescale. Furthermore, it is found that the peak azimuthal vorticity $|\Psi_\theta|$ at the primary vortex ring core will decay as $t^{*-4/3}$ when the flow is axisymmetric. For plane symmetry cases without a magnetic field, decay speeds of two vortex ring cores are different in the symmetric plane. When the magnetic field is applied, the decay of azimuthal vorticity $|\Psi_\theta|$ becomes faster.

ACKNOWLEDGMENTS

The authors gratefully acknowledge the support from the National Natural Science Foundation of China (Grants No. 51927812, 52006212), the Basic Frontier Science Research Program of Chinese Academy of Sciences (Grant No. ZDBS-LY-JSC033), National Key Research and Development Program of China (Grant No.2017YFE0301300), and China Postdoctoral Science Foundation Funded Project (Grant No. 2019M650815).

[1] S. C. R. Dennis and J. D. A. Walker, Numerical solutions for time-dependent flow past an impulsively started sphere, Phys. Fluids **15**, 517 (1972).

[2] T. Sano, Unsteady flow past a sphere at low Reynolds number, J. Fluid Mech. **112**, 433 (1981).

[3] P. M. Lovalenti and J. F. Brady, The hydrodynamic force on a rigid particle undergoing arbitrary time-dependent motion at small Reynolds number, J. Fluid Mech. **256**, 561 (1993).

[4] R.-W. Mei, History force on a sphere due to a step change in the free-stream velocity, Int. J. Multiphase Flow **19**, 509 (1993).
[5] A. B. Basset, *A Treatise on Hydrodynamics: With Numerous Examples*, Vol. 2 (Deighton, Bell and Company, Dover, 1888).
[6] R. Bouard and M. Coutanceau, The early stage of development of the wake behind an impulsively started cylinder for $40 \leqslant Re \leqslant 10^4$, J. Fluid Mech. **101**, 583 (1980).
[7] P. Koumoutsakos and A. Leonard, High-resolution simulations of the flow around an impulsively started cylinder using vortex methods, J. Fluid Mech. **296**, 1 (1995).
[8] X.-G. Wang and C. Dalton, Numerical solutions for impulsively started and decelerated viscous flow past a circular cylinder, Int. J. Numer. Methods Fluids **12**, 383 (1991).
[9] G. J. Sheard, T. Leweke, M. C. Thompson, and K. Hourigan, Flow around an impulsively arrested circular cylinder, Phys. Fluids **19**, 083601 (2007).
[10] E. J. Chang and M. R. Maxey, Unsteady flow about a sphere at low to moderate Reynolds number. Part 2. Accelerated motion, J. Fluid Mech. **303**, 133 (1995).
[11] C. J. Lawrence and R.-W. Mei, Long-time behaviour of the drag on a body in impulsive motion, J. Fluid Mech. **283**, 307 (1995).
[12] M. C. Thompson, T. Leweke, and K. Hourigan, Sphere-wall collisions: Vortex dynamics and stability, J. Fluid Mech. **575**, 121 (2007).
[13] T. Maxworthy, The structure and stability of vortex rings, J. Fluid Mech. **51**, 15 (1972).
[14] T. Maxworthy, Some experimental studies of vortex rings, J. Fluid Mech. **81**, 465 (1977).
[15] J. J. Allen, Y. Jouanne, and B. N. Shashikanth, Vortex interaction with a moving sphere, J. Fluid Mech. **587**, 337 (2007).
[16] Y. B. Kolesnikov and A. B. Tsinober, Experimental investigation of two-dimensional turbulence behind a grid, Fluid Dyn. **9**, 621 (1974).
[17] N. Kanaris, X. Albets, D. Grigoriadis, and S. Kassinos, Three-dimensional numerical simulations of magnetohydrodynamic flow around a confined circular cylinder under low, moderate, and strong magnetic fields, Phys. Fluids **25**, 074102 (2013).
[18] W. Chester, The effect of a magnetic field on Stokes flow in a conducting fluid, J. Fluid Mech. **3**, 304 (1957).
[19] G. Yonas, Measurements of drag in a conducting fluid with an aligned field and large interaction parameter, J. Fluid Mech. **30**, 813 (1967).
[20] J. Delacroix and L. Davoust, Drag upon a sphere suspended in a low magnetic-Reynolds number MHD channel flow, Phys. Rev. Fluids **3**, 123701 (2018).
[21] J.-H. Pan, N.-M. Zhang, and M.-J. Ni, The wake structure and transition process of a flow past a sphere affected by a streamwise magnetic field, J. Fluid Mech. **842**, 248 (2018).
[22] J.-H. Pan, N.-M. Zhang, and M.-J. Ni, Wake structure of laminar flow past a sphere under the influence of a transverse magnetic field, J. Fluid Mech. **873**, 151 (2019).
[23] J.-H. Pan, N.-M. Zhang, and M.-J. Ni, Instability and transition of a vertical ascension or fall of a free sphere affected by a vertical magnetic field, J. Fluid Mech. **859**, 33 (2019).
[24] P. A. Davidson, *An Introduction to Magnetohydrodynamics* (Cambridge University Press, Cambridge, 2001).
[25] R. J. Moreau, *Magnetohydrodynamics* (Springer Science & Business Media, Berlin, 2013).
[26] M.-J. Ni, R. Munipalli, P. Huang, N. B. Morley, and M. A. Abdou, A current density conservative scheme for incompressible MHD flows at a low magnetic Reynolds number. Part II: On an arbitrary collocated mesh, J. Comput. Phys. **227**, 205 (2007).
[27] B. Mück, C. Günther, U. Müller, and L. Bühler, Three-dimensional MHD flows in rectangular ducts with internal obstacles, J. Fluid Mech. **418**, 265 (2000).
[28] A. G. Tomboulides and S. A. Orszag, Numerical investigation of transitional and weak turbulent flow past a sphere, J. Fluid Mech. **416**, 45 (2000).
[29] T. A. Johnson and V. C. Patel, Flow past a sphere up to a Reynolds number of 300, J. Fluid Mech. **378**, 19 (1999).

[30] P. P. Brown and D. F. Lawler, Sphere drag and settling velocity revisited, J. Environ. Eng. **129**, 222 (2003).
[31] R. Clift, J. R. Grace, and M. E. Weber, *Bubbles, Drops, and Particles* (Academic Press, New York, 2005).
[32] R. Turton and O. Levenspiel, A short note on the drag correlation for spheres, Powder Technol. **47**, 83 (1986).